ELSEVIER

Contents lists available at ScienceDirect

## Computers and Geotechnics

journal homepage: www.elsevier.com/locate/compgeo



Research Paper

# Small-strain shear modulus of granular materials and its dependence on stress states and fabric



Mingjin Jiang, Jun Yang

Department of Civil Engineering, The University of Hong Kong, Pokfulam Road, Hong Kong, China

#### ARTICLE INFO

Keywords: Small-strain shear modulus Discrete element method Granular materials Triaxial tests Mechanical coordination number Fabric anisotropy

#### ABSTRACT

This paper presents a comprehensive study on the evolution of the small-strain shear modulus (G) of granular materials during hydrostatic compression, conventional triaxial, reduced triaxial, and p-constant triaxial tests using 3D discrete element method. Results from the hydrostatic compression tests indicate that G can be precisely estimated using Hardin's equation and that a linear correlation exists between a stress-normalized G and a function of mechanical coordination number and void ratio. During the triaxial tests, the specimen fabric, which refers to the contact network within the particle assembly, remains almost unchanged within a threshold range of stress ratio (SR). The disparity between measured G and predicted G, as per empirical equations, is less than 10% within this range. However, once this threshold range is exceeded, G experiences a significant SR effect, primarily due to considerable adjustments in the specimen's fabric. The study concludes that fabric information becomes crucial for accurate G prediction when SR threshold is exceeded. A stiffness-stress-fabric relationship spanning a wide range of SR is put forward by incorporating the influences of redistribution of contact forces, effective connectivity of fabric, and fabric anisotropy into the empirical equation.

## 1. Introduction

The term "small-strain shear modulus" refers to the shear modulus at extremely small strain levels, typically below  $10^{-5}$ . It is a basic soil property with clear physical meaning and has a wide range of applications in geotechnical engineering (Yang, 2024), including earthquake ground response analyses, underground construction, and liquefaction potential assessment (Burland and Kalra, 1986; Andrus and Stokoe, 2000; Clayton and Heymann, 2001; Zhou and Chen, 2007; Yang and Yan, 2009). The pioneering research on the small-strain shear modulus, G, of soil was carried out by Hardin and Richart (1963). They performed resonant column tests on granular soils and discovered that G in an isotropic stress state relies primarily on the void ratio, e, and effective confining stress,  $\sigma'_0$ . Subsequent studies confirmed their observation and led to a general form for G (Kuribayashi et al., 1975; Iwasaki and Tatsuoka, 1977; Kokusho, 1980; Saxena and Reddy, 1989):

$$G = AF(e) \left(\sigma_0'/p_a\right)^{\alpha} \tag{1}$$

where *A* denotes a constant depending on the type of soil; F(e) is a function of void ratio and can be expressed as  $F(e) = (B - e)^2/(1 + e)$  and *B* is typically taken as 2.17 for round particles;  $p_a$  marks a reference

stress;  $\alpha$  designates the stress exponent.

Although isotropic stress conditions are commonly employed in laboratory element tests, soils in natural environments often experience anisotropic stress conditions, such as those found in slopes or under foundations. Unlike the case with isotropic stress conditions, a clear consensus regarding the relationship between G and anisotropic stress states remains elusive. Hardin and Black (1966) were the first to note that Eq. (1) is applicable to anisotropic stress states when replacing  $\sigma'_0$  with the mean effective stress, p':

$$G = AF(e)(p'/p_a)^{\alpha} \tag{2}$$

The validity of Eq. (2) has been upheld by experimental evidence under triaxial stress conditions (Kuribayashi et al., 1975; Schmertmann, 1978; Tatsuoka et al., 1979). However, some researchers reported that G is solely determined by the mean effective stress in the wave polarization plane, relatively independent of the principal effective stress in the out-of-plane direction (Knox et al., 1982; Yu and Richart, 1984; Santamarina and Cascante, 1996). Hence, it can be expressed as (Chen and Yang, 2024):

E-mail address: junyang@hku.hk (J. Yang).

<sup>\*</sup> Corresponding author.

$$G_{ij} = AF(e) \left(\frac{\sigma_i' + \sigma_j'}{2p_a}\right)^{\alpha} \tag{3}$$

where  $\sigma_i$  and  $\sigma_j$  are the principal effective stresses in the i and j direction, i.e., the wave propagation and oscillation directions, respectively. The third perspective posits that it is not the mean principal stress, but the respective component of the principal effective stress in the polarization plane, which has the major influence on G (Roesler, 1979; Yu and Richart, 1984; Hardin and Blandford, 1989; Santamarina and Cascante, 1996; Rampello et al., 1997; Dutta et al., 2021). Mathematically it can be described as follows (Yang, 2024):

$$G_{ij} = AF(e)p_a^{-\alpha_a - \alpha_b}\sigma_i^{\alpha_a}\sigma_i^{\alpha_b} \tag{4}$$

where  $\alpha_a$  and  $\alpha_b$  are stress exponents of  $\sigma_i$  and  $\sigma_j$ , respectively. Nevertheless, However, it remains an open question whether  $\sigma_i$  and  $\sigma_j$  contribute equally to the associate  $G_{ij}$ , i.e.,  $\alpha_a = \alpha_b$ . Some researchers deemed that  $\alpha_a \neq \alpha_b$  (Roesler, 1979; Yu and Richart, 1984; Santamarina and Cascante, 1996), while others suggested that  $\alpha_a = \alpha_b$  and Eq. (4) can be simplified as (Hardin and Blandford, 1989; Rampello et al., 1997; Dutta et al., 2021):

$$G_{ij} = AF(e) \left( \sqrt{\sigma'_i \sigma'_j} / p_a \right)^a$$
 (5)

In addition, Bellotti et al. (1996) modified Eq. (4) to account for the influence of effective principal stress in the third direction:

$$G_{ij} = AF(e)p_a^{-\alpha_a - \alpha_b - \alpha_c} \sigma_i^{\alpha_a} \sigma_j^{\alpha_b} \sigma_k^{\alpha_c}$$

$$\tag{6}$$

where  $\sigma_k$  is the third (i.e., out-of-plane) principal effective stress, and  $\alpha_c$  denotes the stress exponent of  $\sigma_k$ . This Equation was also adopted by Kuwano and Jardine (2002) in a different form. However, it is crucial to point out that  $\alpha_c$  is remarkably smaller  $\alpha_a$  and  $\alpha_b$ .

Despite the difference in empirical equations, the influence of stress ratio (SR) on G has been widely observed. For instance, Kuribayashi et al. (1975) found their test results could not be explained by Eq. (2) when SR was greater than 2.5 under triaxial compression conditions. Similarly, Tatsuoka et al. (1979) reported that the effect of SR on G became significant when SR > 4 in triaxial compression cases. Yu and Richart (1984) observed that when SR was larger than 2.4–3.0, the effect of SR on G was greater than 10 %. Kuwano and Jardine (2002) discovered that G was distinctly lower than expected when SR was above 2.2. To account for the effect of SR, various correction factors have been proposed and integrated into empirical equations, e.g., factor  $K_n$  proposed by Yu and Richart (1984), factor ( $\eta+1$ ) given by Payan et al. (2016), and factor R suggested by Chen and Yang (2024).

It is widely recognized that the macroscopic properties of granular materials are closely related to the underlying microscopic fabric (Chang et al., 1995; Thornton, 2000; Magnanimo et al., 2008; Yimsiri and Soga, 2010; Yang and Dai, 2011; Gu and Yang, 2013; Guo and Zhao, 2013; Otsubo et al., 2020; Zhang and Yang, 2023). Fabric typically refers to the contact network when it comes to the stiffness of granular materials. In the empirical equations previously mentioned, factor A represents G/F(e) measured in a reference isotropic stress state of  $p_a$ , and the stress component exponents (e.g.,  $\alpha$ ) stem from the sensitivity of G to stress states. Given that G is a constant-fabric measurement in a specific stress state, and that A and stress exponents are determined by fitting the power function to G in different anisotropic stress states, the influence of both inherent soil fabric and changes in soil fabric during loading are intrinsically factored in (Cha et al., 2014). As previous studies included different testing materials, shape of specimens, and stress paths, the resulting variances in soil fabric may have led to differing results, thus contributing to the variety of empirical equations. Moreover, under substantial deviatoric stress, granular materials may undergo significant adjustments in microscopic structure (Oda, 1972; Hasan and Alshibli, 2012; Schmidt et al., 2022), which could account for the observed

effects of SR in experimental studies (Kuwano and Jardine, 2002). Therefore, fabric information is crucial for accurately determining and comprehending the G of granular materials in anisotropic stress states.

Several advanced scanning techniques such as scanning electron microscopy and X-ray Computed Tomography, along with testing methods like the photo-elastic experiment, have been employed to measure the fabric of granular materials (Majmudar and Behringer, 2005; Mitaritonna et al., 2014; Wiebicke et al., 2020). Nonetheless, the practical application of these technologies can be complex, timeconsuming, labor-intensive, and expensive. Meanwhile, the discrete element method (DEM), pioneered by Cundall and Strack (1979), provides a convenient approach to conduct a comprehensive quantitative assessment of fabric throughout the testing procedure. This method has become increasingly popular in the study of small-strain stiffness. For example, Wang and Mok (2008) conducted both experimental and DEM studies on the anisotropy of G, demonstrating that G exhibits relative independence from the out-of-plane stress. Gu et al. (2013) performed triaxial tests using 2D DEM and discovered that the fabric of granular materials remains nearly constant within a specific SR range. However, if SR surpasses this range, the fabric adjusts significantly to resist anisotropic stresses. O'Donovan et al. (2015) executed the DEM simulation with a face-centered cubic assembly, claiming that the principal effective stress out-of-plane has a finite impact on G. Nguyen et al. (2018) confirmed the relationship between  $G_{ij}$  and  $\sqrt{\sigma_i'\sigma_j'}$  through DEM simulation of true triaxial tests. Gu et al. (2023) measured the shear wave velocities in conventional triaxial and true triaxial tests by DEM, showing the dependency of stress normalized shear wave velocities (or G) on the contact normal densities in the wave propagation and particle oscillation directions. Gong et al. (2024) explored the effects of particle shape, physical properties and particle size distribution on G in isotropic stress states through DEM. They found that G uniquely depends on the mechanical coordination number and contact stiffness, suggesting an empirical expression to depict their relationship.

With the help of DEM, significant progress has been made in understanding the relationship between the small-strain shear modulus, stress states, and fabric. For example,  $G_{ij}$  tends to be proportional to  $\sqrt{\sigma_i'\sigma_j'}$ , and is affected by the distribution of contact force, contact normal, and coordination number (Gu et al., 2017; Nguyen et al., 2018; Gong et al., 2019; Otsubo et al., 2020; Liu et al., 2023). However, previous studies have typically encompassed a limited array of stress combinations or stress paths, and the inconsistencies identified in these studies have not been thoroughly resolved. These constraints have muddled the clarity of their data and affected the generality of their conclusions. Moreover, the accuracy of these empirical equations may be compromised due to adjustments in fabric (Gu et al., 2023). Consequently, it is imperative to further investigate the relationship between the small-strain shear modulus, stress states, and fabric.

To gain a comprehensive perception of the small-strain shear modulus of granular materials under various stress conditions and to explore the quantitative stiffness-stress-fabric relationship, we carried out systematic DEM simulations on the randomly packed samples. These simulations encompassed a variety of tests, including hydrostatic compression (HC), conventional triaxial (CT), reduced triaxial (RT), and p-constant triaxial (PT) tests. Concurrently, G of the specimen and corresponding microstructure were monitored. The new contributions of this study are: (a) an attempt to reconcile the divergent views in the literature concerning the impact of anisotropic stress states on the small-strain shear modulus, and to introduce a factor,  $R_{\rm c}$ , to account for the SR effect arising from the redistribution of contact forces; (b) a proposal of a quantitative relationship linking the small-strain shear modulus with anisotropic stress states and the fabric of granular materials across an extensive range of SR.

#### 2. Simulation Method

#### 2.1. Specimen Generation

In a DEM simulation, the selection of contact model is significant. We adopted a simplified Hertz-Mindlin contact model, as depicted in Fig. 1, to capture the stress-dependent stiffness (Jiang and Yang, 2024). The contact force, F, which comprises the hertz force and dashpot force, can be decomposed into the normal and tangential components. The normal hertz force,  $F_n^h$ , can be formulated as follows:

$$F_{\rm n}^{\rm h} = \frac{2}{3}k_{\rm n}\delta_{\rm n} \tag{7}$$

where  $k_n$  is the tangent elastic stiffness in the normal direction;  $\delta_n$  denotes normal contact overlap. The tangential hertz force,  $F_t^h$ , is restrained by the law of Coulomb friction, which can be expressed as:

$$(F_{t}^{h})^{T} = \begin{cases} (F_{t}^{h})^{T-1} - k_{t} \Delta \delta_{t}, (F_{t}^{h})^{T} \leq \mu F_{n}^{h} \\ \mu F_{n}^{h}, & \text{else} \end{cases}$$
 (8)

where  $\left(F_{\rm t}^{\rm h}\right)^T$  and  $\left(F_{\rm t}^{\rm h}\right)^{T-1}$  are the tangential hertz force at current time step, T, and former time step, T-1, respectively;  $k_{\rm t}$  represent the tangent elastic stiffness in the tangential directions;  $\Delta\delta_{\rm t}$  indicates the relative tangential displacement increment;  $\mu$  signifies the friction coefficient. The normal dashpot force,  $F_{\rm n}^{\rm d}$ , and tangential dashpot force,  $F_{\rm t}^{\rm d}$ , are updated by:

$$\begin{cases} F_{n}^{d} = -c_{n}\dot{\delta}_{n} \\ F_{t}^{d} = -c_{t}\dot{\delta}_{t} \end{cases}$$
 (9)

where  $c_n$  and  $c_t$  represent the normal and tangential viscous damping coefficients, respectively;  $\dot{\delta}_n$  and  $\dot{\delta}_t$  denote the relative translational velocity in the normal and tangential directions, respectively.

We carried out the DEM simulations utilizing PFG<sup>3D</sup> (Itasca Consulting Group, 2015). Cubic specimens, comprising 12,991 spherical particles, were used, which adhered to the particle size distribution of Ottawa 50–70 sand, as illustrated in Fig. 1. The specimen's coefficient of uniformity,  $C_{\rm u}$ , measured 1.23, and the mean particle diameter,  $d_{50}$ , is 0.26 mm. The radius expansion method was utilized to generate the specimen. To begin, spherical particles were randomly generated within a cubic space measuring 6 mm on each side, bounded by three pairs of frictionless walls. These particles were initially set to half their intended size, then underwent gradual enlargement to attain their final sizes. Following this, the newly formed assembly was subjected to isotropic

compression until it achieved a stress condition of 10 kPa. Notably, the local damping coefficient was set to 0.7 to expedite the attainment of equilibrium, and different inter-particle friction coefficients were used during this process to generate the specimen with different e. Subsequently, the inter-particle friction coefficient was adjusted to 0.5, the local damping was removed, and the normal critical damping ratio was set at 0.1. The specimen was then further isotropically compressed to achieve an initial stress level of 100 kPa. Interim inter-particle friction coefficients of 0 and 0.2 were used to generate a dense specimen with an initial e-value of 0.6192 and a loose specimen with an initial e-value of 0.7384. These e values correspond to relative densities of 100 % and 20.1 %, respectively. The specimen with the maximum initial e-value of 0.7684 was prepared using an interim inter-particle friction coefficient of 0.5. The final dimensions are 5.83 mm and 5.69 mm on each side for the loose and dense specimens, respectively. The study of Wiacek and Molenda (2016) suggests that a granular packing dimension of at least 15 times the mean particle diameter is sufficient to minimize wall effects and ensure representative average values. Since the specimen dimensions in this study exceed  $20d_{50}$ , the influence of size effects can be considered negligible.

In our DEM simulations, the material property parameters were set to match the typical values of natural quartz grains, which has been widely adopted in prior studies (Ng and Petrakis, 1996; Gu et al., 2017; Liu et al., 2023; Gong et al., 2024; Jiang and Yang, 2024). The detailed parameters used in the specimen are summarized in Table 1. Consequently, at the initial stress level of 100 kPa, G is approximately 180 MPa for the dense specimen and 100 MPa for the loose specimen. These values of G were measured using the probe test, the methodology of which is introduced in detail in the following section.

#### 2.2. Stress path and probe test

The specimen was initially isotropically compressed from 100 to

Table 1
Parameters used in the simulation.

Particle shape	Spherical	No. of particles	12,991
Contact law	Hertz- Mindlin	Particle density	2660 kg/ m <sup>3</sup>
Wall shear modulus	29 GPa	Particle shear modulus	29 GPa
Wall Poisson's ratio	0.15	Particle Poisson's ratio	0.15
Wall-particle friction coefficient	0	Inter-particle friction coefficient	0.5
Normal critical damping ratio	0.1	Tangential critical damping ratio	0
Local damping coefficient	0	Gravity	0 m/s <sup>2</sup>

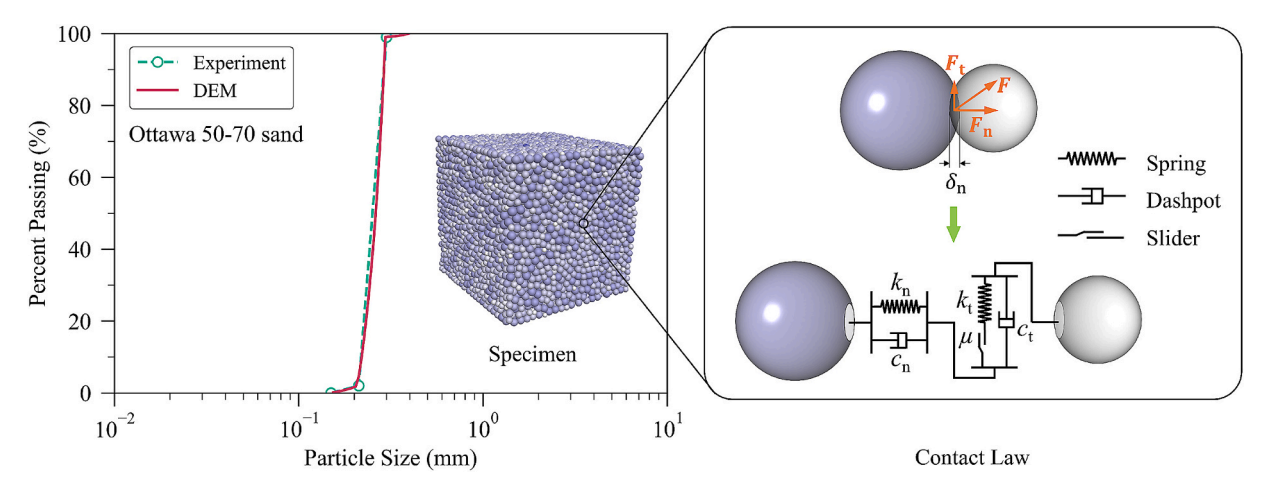


Fig. 1. Particle size distribution and contact law in DEM specimen (Experiment result from Chen and Yang (2024)).

1000 kPa to create a reference dataset. Then, from isotropic stress states of 100, 200, 500, and 1000 kPa, consolidation was implemented along different stress paths to achieve the target anisotropic stress states. These stress paths include CT, RT, and PT tests, as shown in Fig. 2. In the CT stress path, the stresses in the horizontal directions,  $\sigma_{\rm h}'$  (i.e.,  $\sigma_{\rm x}'$  and  $\sigma_{\rm y}'$ ), were maintained constant while the stress in the vertical directions,  $\sigma'_{v}$ (i.e.,  $\sigma_{z}'$ ), was gradually increased for conventional triaxial compression (CTC);  $\sigma'_{v}$  remained constant while  $\sigma'_{h}$  was progressively increased for conventional triaxial extension (CTE). In the RT stress path,  $\sigma'_{v}$  was kept constant while  $\sigma_h'$  was monotonically decreased for reduced triaxial compression (RTC);  $\sigma'_h$  was held constant while  $\sigma'_v$  was successively decreased for reduced triaxial extension (RTE). Furthermore, in the PT stress path, p' stayed constant while  $\sigma'_{\rm h}$  decreased and  $\sigma'_{\rm v}$  increased simultaneously for p-constant triaxial compression (PTC); p' guaranteed constant while  $\sigma'_{\rm h}$  increased and  $\sigma'_{\rm v}$  decreased coterminously for p-constant triaxial extension (PTE). Particularly, SR is defined as  $\sigma_{\rm v}'/\sigma_{\rm h}'$  in this study.

The test programs are summarized in Table 2. Here, the test ID is named according to the loading path, the density of specimen, and stress level. For instance, "HC-L" signifies a HC stress path applied to the loose specimen; "CTC-D1" represents a CTC stress path initiated from the lowest stress level (i.e., 100 kPa) for the dense specimen. The mean effective stress, p', and deviatoric stress, q, are defined as

$$\begin{cases}
 p' = (\sigma'_{x} + \sigma'_{y} + \sigma'_{z})/3, \\
 q = \sqrt{\left[\left(\sigma'_{x} - \sigma'_{y}\right)^{2} + \left(\sigma'_{y} - \sigma'_{z}\right)^{2} + \left(\sigma'_{z} - \sigma'_{x}\right)^{2}\right]/2}
\end{cases} (10)$$

The dimensionless parameter—inertia number, I, has been extensively utilized to identify the flow regime of granular materials (da Cruz et al., 2005; Peyneau and Roux, 2008; Perez et al., 2016). It denotes as  $I=|\dot{e}|d_{50}\sqrt{\rho_s/p'}$ , where  $\dot{e}$  is the strain rate and  $\rho_s$  refers to the particle density. The response of the granular assembly is generally considered quasi-static, with negligible inertial effects, when I falls below  $10^{-3}$  (van der Elst et al., 2012). During the tests, the target stress state was achieved by moving the boundary walls with a servo system. To ensure a quasi-static response, the maximum velocity of the walls was limited to 0.05 mm/s, thus keeping the inertia number far smaller than  $10^{-3}$ .

The probe test was performed at specific intervals, with the probing

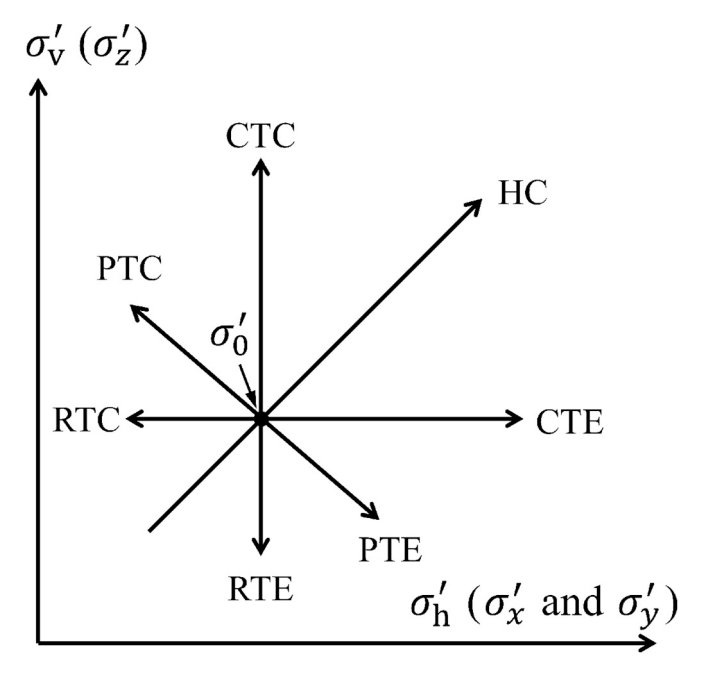


Fig. 2. Stress path of HC, CT, RT, and PT tests.

frequency documented in Table 2. Noting that under anisotropic stress states, the simple-shear-type probe test is a more appropriate and reliable method for measuring small-strain shear modulus compared with the triaxial-type probe test, the  $G_{ki}$  in the ki plane is determined using the equation below:

$$G_{ki} = \Delta \tau_{ki} / \Delta \gamma_{ki} \tag{11}$$

where  $\Delta \tau_{ki}$  and  $\Delta \gamma_{ki}$  are the stress increment and strain increment in the ki plane, respectively. The probe test continues until the shear strain increment reaches  $10^{-6}$ . During the probe tests, the shear strain rate is maintained at  $10^{-3}$ /s, ensuring that the inertia number remains smaller than  $10^{-8}$ . In addition, as suggested by Cundall et al. (1989), the interparticle friction coefficient was assigned an infinite value during the probe test. This strategy was employed to inhibit sliding between particles and thereby rule out plastic deformation of the specimen.

## 3. Results and Analysis

#### 3.1. HC tests

The evolution of G during HC tests is depicted in Fig. 3. As shown in Fig. 3(a), G in different directions exhibit near-identical values, suggesting isotropy within the specimen. Moreover, as expected, G increases with the increasing confining pressure. Fig. 3(b) demonstrates that G/F(e) has a strong power relationship with  $\sigma'_0/p_a$ , where  $F(e) = (1.22 - e)^2/(1 + e)$  and  $p_a = 1$  kPa. This relationship aligns with Hardin's equation, as formulated in Eq. (1), with the constant B = 1.22 to give a unified relationship for both loose and dense specimens.

The increase of shear modulus is concurrent with the adjustment of specimen fabric. As shown in Fig. 4(a), e declines while the mechanical coordination number,  $Z_{\rm m}$ , ascends with the increasing confining pressure.  $Z_{\rm m}$  represents the coordination number considering only mechanically stable particles, and is defined as (Thornton, 2000):

$$Z_{\rm m} = \frac{2N_{\rm c} - N_{\rm p}^1}{N_{\rm p} - N_{\rm p}^1 - N_{\rm p}^0} \tag{12}$$

where  $N_{\rm c}$  is the number of contact point;  $N_{\rm p}$  denotes the number of particles;  $N_{\rm p}^1$  and  $N_{\rm p}^0$  designate the number of particles maintaining a single contact and devoid of any contact with other entities, respectively. Previous studies have demonstrated that G is closely linked to  $Z_{\rm m}$  under hydrostatic conditions. For instance, linear relationships have been established between  $G/\sigma_0^{-1/3}$  and  $(Z_{\rm m}/e)^{2/3}$  (Nie et al., 2022). This linear relationships were also observed in this study as shown in Fig. 4 (b), underscoring the close interplay between the small-strain shear modulus, stress states, and fabric of granular materials.

## 3.2. Triaxial tests

CT, RT, and PT tests were initiated from isotropic stress states of 100, 200, 500, and 1000 kPa. Given similar results across various initial stress levels, we present only one portion here for brevity. As shown in Fig. 5 (a-c), G can vary significantly in different planes due to the anisotropic stress states. Especially, the degree of anisotropy in G escalates with increasing stress anisotropy. In different stress paths,  $G_{yz}$  and  $G_{zx}$  can be considered identical, suggesting the transversely isotropic symmetry of the specimen. Gu et al. (2013, 2017) reported that there are threshold values of SR, termed as SRth, along the RTE/CTC. Within the ranges demarcated by two  $SR_{th}$ , the coordination number, Z, or mechanical coordination number,  $Z_{\rm m}$ , exhibits minimal variation; however, when SR surpasses this range, a significant reduction in Z or  $Z_m$  was observed. This trend is also visible in all triaxial stress paths in our study, as shown in Fig. 5(d-f). Especially for the dense specimen,  $Z_{\rm m}$  remains nearly constant as the SR resides the range between two threshold values. The change in *G* is contingent on the variation of stress level. Nevertheless,

Computers and Geotechnics 183 (2025) 107183

**Table 2**Summary of test programs.

Test ID	Initial state	2			Final state				Test ID	Initial state	2			Final state				Probing frequency
	p'(kPa)	q (kPa)	e	SR	p'(kPa)	q (kPa)	e	SR		p'(kPa)	q (kPa)	e	SR	p'(kPa)	q (kPa)	e	SR	
HC-D	100.0	0	0.6192	1.0	1000.0	0	0.6143	1.00	HC-L	100.0	0	0.7384	1.0	1000.0	0	0.7319	1.0	per 100 kPa*
CTC-D1	100.0	0	0.6192	1.0	146.7	140.0	0.6188	2.40	CTC-L1	100.0	0	0.7384	1.0	120.0	60.0	0.7381	1.60	per 10 kPa
CTE-D1					193.3	140.0	0.6184	0.42	CTE-L1					140.0	60.0	0.7379	0.63	per 10 kPa
RTC-D1					63.3	55.0	0.6195	2.22	RTC-L1					76.7	35.0	0.7387	1.54	per 5 kPa
RTE-D1					80.0	60.0	0.6194	0.40	RTE-L1					86.7	40.0	0.7386	0.60	per 5 kPa
PTC-D1					100.0	95.5	0.6192	2.40	PTC-L1					100.0	50.0	0.7384	1.60	per 0.1 SR
PTE-D1					100.0	75.0	0.6192	0.40	PTE-L1					100.0	46.2	0.7384	0.60	per 0.1 <i>SR</i>
CTC-D2	200.0	0	0.6184	1.0	293.3	280.0	0.6178	2.40	CTC-L2	200.0	0	0.7374	1.0	240.0	120.0	0.7369	1.60	per 20 kPa
CTE-D2					386.7	280.0	0.6172	0.42	CTE-L2					280.0	120.0	0.7366	0.63	per 20 kPa
RTC-D2					126.7	110.0	0.6189	2.22	RTC-L2					153.3	70.0	0.7378	1.54	per 10 kPa
RTE-D2					160.0	120.0	0.6187	0.40	RTE-L2					173.3	80.0	0.7375	0.60	per 10 kPa
PTC-D2					200.0	190.9	0.6184	2.40	PTC-L2					200.0	100.0	0.7373	1.60	per 0.1 SR
PTE-D2					200.0	150.0	0.6184	0.40	PTE-L2					200.0	92.3	0.7373	0.60	per 0.1 <i>SR</i>
CTC-D3	500.0	0	0.6166	1.0	733.3	700.0	0.6155	2.40	CTC-L3	500.0	0	0.7349	1.0	600.0	300.0	0.7341	1.60	per 50 kPa
CTE-D3					966.7	700.0	0.6145	0.42	CTE-L3					700.0	300.0	0.7335	0.63	per 50 kPa
RTC-D3					316.7	275.0	0.6176	2.22	RTC-L3					383.3	175.0	0.7357	1.54	per 25 kPa
RTE-D3					400.0	300.0	0.6172	0.40	RTE-L3					433.3	200.0	0.7353	0.60	per 25 kPa
PTC-D3					500.0	477.3	0.6166	2.40	PTC-L3					500.0	250.0	0.7348	1.60	per 0.1 <i>SR</i>
PTE-D3					500.0	375.0	0.6166	0.40	PTE-L3					500.0	230.8	0.7348	0.60	per 0.1 <i>SR</i>
CTC-D4	1000.0	0	0.6143	1.0	1466.7	1400.0	0.6126	2.40	CTC-L4	1000.	0 0	0.7319	1.0	1200.0	600.0	0.7307	1.6	0 per 100 kPa
CTE-D4					1933.3	1400.0	0.6110	0.42	CTE-L4					1400.0	600.0	0.7297	0.6	3 per 100 kPa
RTC-D4					633.3	550.0	0.6159	2.22	RTC-L4					766.7	350.0	0.7331	1.5	4 per 50 kPa
RTE-D4					800.0	600.0	0.6152	0.40	RTE-L4					866.7	400.0	0.7325	0.6	0 per 50 kPa
PTC-D4					1000.0	954.5	0.6144	2.40	PTC-L4					1000.0	500.0	0.7318	1.6	•
PTE-D4					1000.0	750.0	0.6144	0.40	PTE-L4					1000.0	461.5	0.7317	0.6	-

<sup>\*</sup>Every 20 kPa when effective stress is from 100 kPa to 200 kPa.

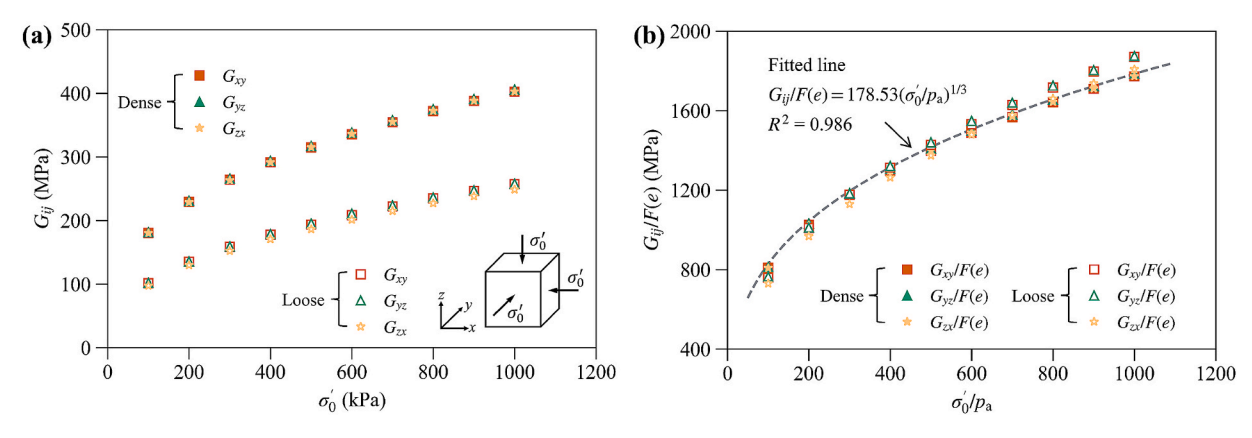


**Fig. 3.** (a) Evolution of G during HC tests and (b) power law between  $G_{ii}/F(e)$  and  $\sigma'_0/p_a$ .

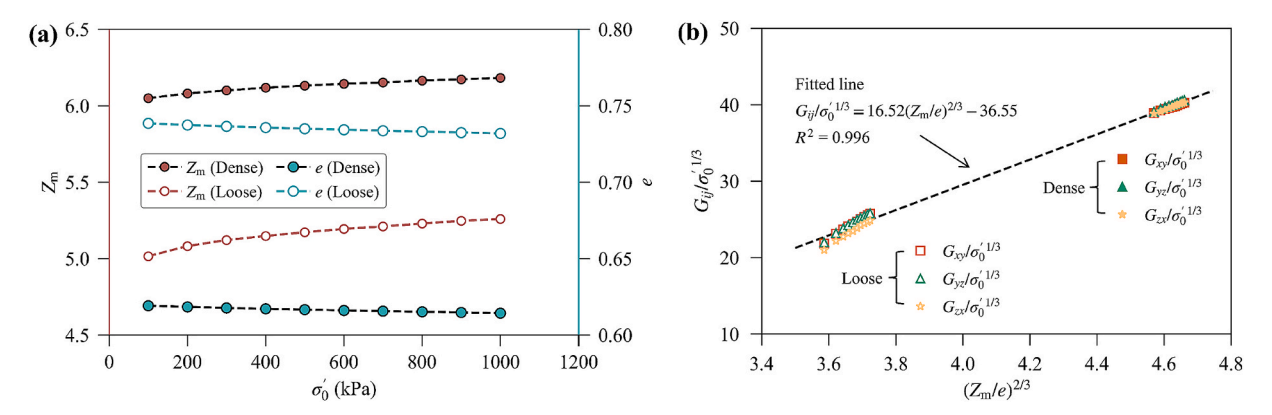


**Fig. 4.** (a) Evolution of e and  $Z_m$ ; (b)  $G_{ij}/\sigma'_0$  vs.  $(Z_m/e)^{2/3}$  during HC tests ( $G_{ij}$  in MPa and  $\sigma'_0$  in kPa).

irrespective of the plane they are in, a marked decline in G is correlated with a decrease in  $Z_{\rm m}$  when SR surpasses its threshold values.

Moreover, consistent with  $Z_{\rm m}$ , fabric anisotropy also remains almost constant within the range demarcated by two  $SR_{\rm th}$ , as corroborated by the contact normal probability density and the anisotropy factor,  $a_{\rm r}$ , shown in Fig. 6. The contact normal probability density,  $f(\theta, \varphi)$ , was calculated according to the following formula:

$$f(\theta, \varphi) = \frac{P(\theta_i \le \theta < \theta_{i+1}, \varphi_j \le \varphi < \varphi_{j+1})}{\int_{\varphi_i}^{\varphi_{j+1}} \int_{\theta_i}^{\theta_{i+1}} \theta d\theta d\varphi}$$
(13)

where P denotes the probability of a contact normal pointing to a specific directional range;  $\theta$  and  $\varphi$  are the polar angle and azimuth angle respectively, in the context of spherical coordinates; the subscripts i, i+1, j, and j+1 represent the lower limit and upper limit of the directional range, respectively.

The fabric tensor,  $\Phi$ , is commonly used to evaluate the anisotropic of fabric, defined as (Satake, 1978; Oda, 1982; Barreto et al., 2009; Zhang et al., 2023):

$$\Phi_{ij} = \frac{1}{N_c} \sum_{c=1}^{N_c} n_i^c n_j^c \tag{14}$$

where  $n_i$  and  $n_j$  are the component of a unit contact normal in the i and j directions, respectively. Furthermore, the degree of anisotropy is typically quantified using  $a_r$ , defined as:

$$a_r = \sqrt{\frac{3}{2}D_{ij}D_{ji}} \tag{15}$$

where the deviatoric tensor  $D_{ij}$  denotes as  $D_{ij} = \frac{15}{2} (\Phi_{ij} - \frac{1}{3} \delta_{ij})$ , and  $\delta_{ij}$  is

Kronecker delta. Within the two threshold values of SR, the contact normal probability density in each direction remains almost unchanged, and  $a_r$  values are nearly 0. However, the magnitude of contact normal forces, as also illustrated in Fig. 6, fluctuates with alterations in the principal effective stress, irrespective of the degree of fabric anisotropy. The mean contact normal force refers to the average magnitude of contact normal forces within a designated directional region. Generally, there is a direct correlation between the magnitude of contact normal forces and the principal effective stress in the same direction—as one increases, so does the other, and vice versa.

The results discussed above suggest that the specimen may adjust the distribution of contact forces and its fabric to accommodate changes in stress during triaxial tests. The change in G primarily stems from the redistribution of contact forces when SR lies within its threshold range. While, once SR exceeds this range, both the adjustment of contact force and fabric contribute to the variation of G. The evolution of deviatoric strain,  $\varepsilon_q$ , and volumetric strain  $\varepsilon_v$  also keeps consistent with the adjustment of microscopic structure, as depicted in Fig. 7. Here,

$$\varepsilon_{\rm v} = \varepsilon_{\rm x} + \varepsilon_{\rm y} + \varepsilon_{\rm z} \quad {\rm and} \quad \varepsilon_{\rm q} = \quad \sqrt{\tfrac{2}{9} \left[ \left( \varepsilon_{\rm x} - \varepsilon_{\rm y} \right)^2 + \left( \varepsilon_{\rm x} - \varepsilon_{\rm z} \right)^2 + \left( \varepsilon_{\rm y} - \varepsilon_{\rm z} \right)^2 \right]}.$$

Generally, when SR is within its threshold range,  $\varepsilon_q$  tends to increase linearly, mirroring the changes in SR. However, once SR surpasses its threshold range, the rate at which  $\varepsilon_q$  increases accelerates significantly. The evolution of  $\varepsilon_v$  relies on the change in p'. Specifically, an increase in p' typically leads to the contraction of specimen volume (i.e.,  $\varepsilon_v$  increases). Conversely, a decrease in p' would cause the swell in specimen volume (i.e.,  $\varepsilon_v$  decreases). For the PT tests, since p' remains constant,  $\varepsilon_v$  also stays unchanged accordingly. It is worth noting that as SR increases/decreases beyond its threshold range, the dense specimen tends to dilate, whereas the loose specimen exhibits a tendency to contract. However, due to the limited values of SR were considered in this study,

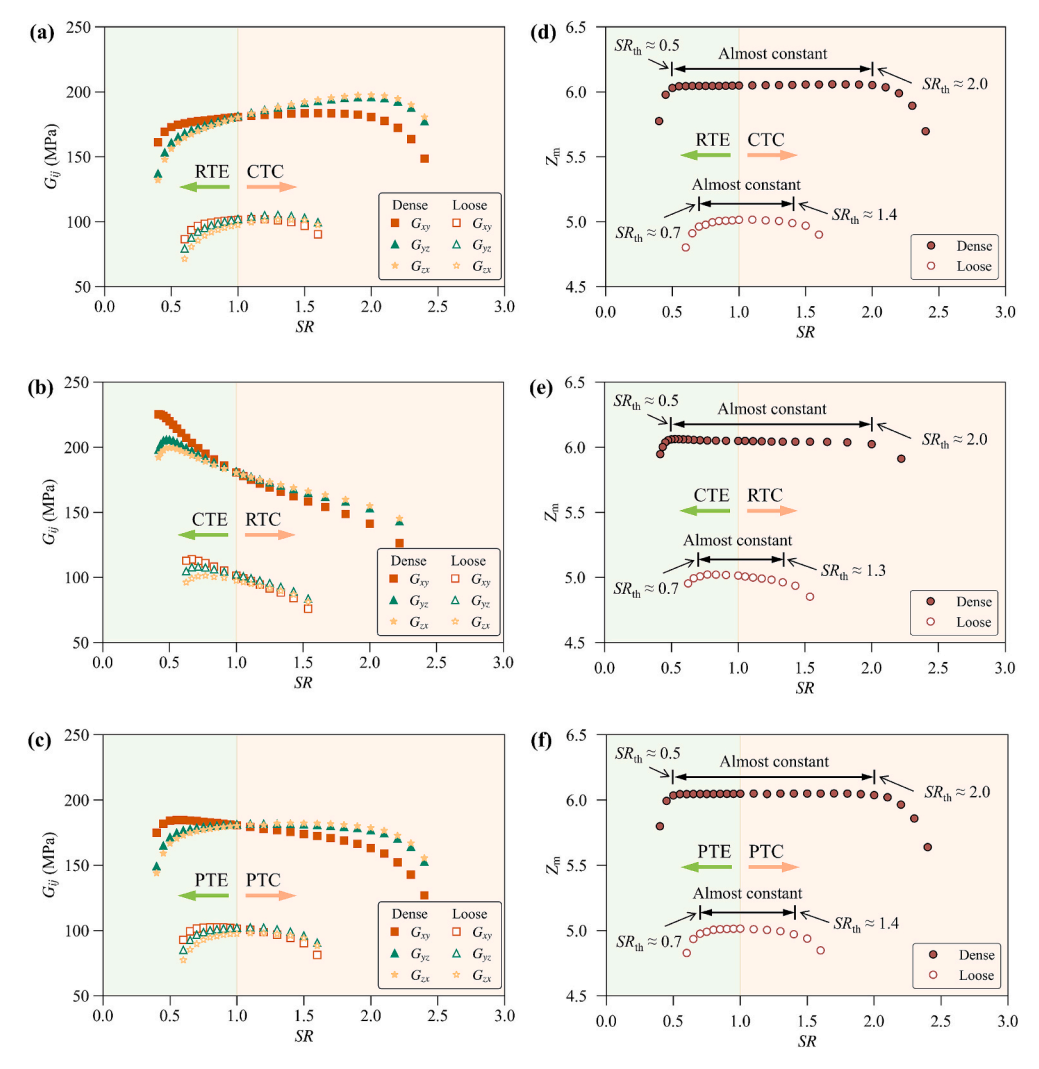


Fig. 5. Evolution of (a–c)  $G_{ij}$  and (d–f)  $Z_{im}$  with SR during CT, RT, and PT tests initialed from the stress level of 100 kPa.

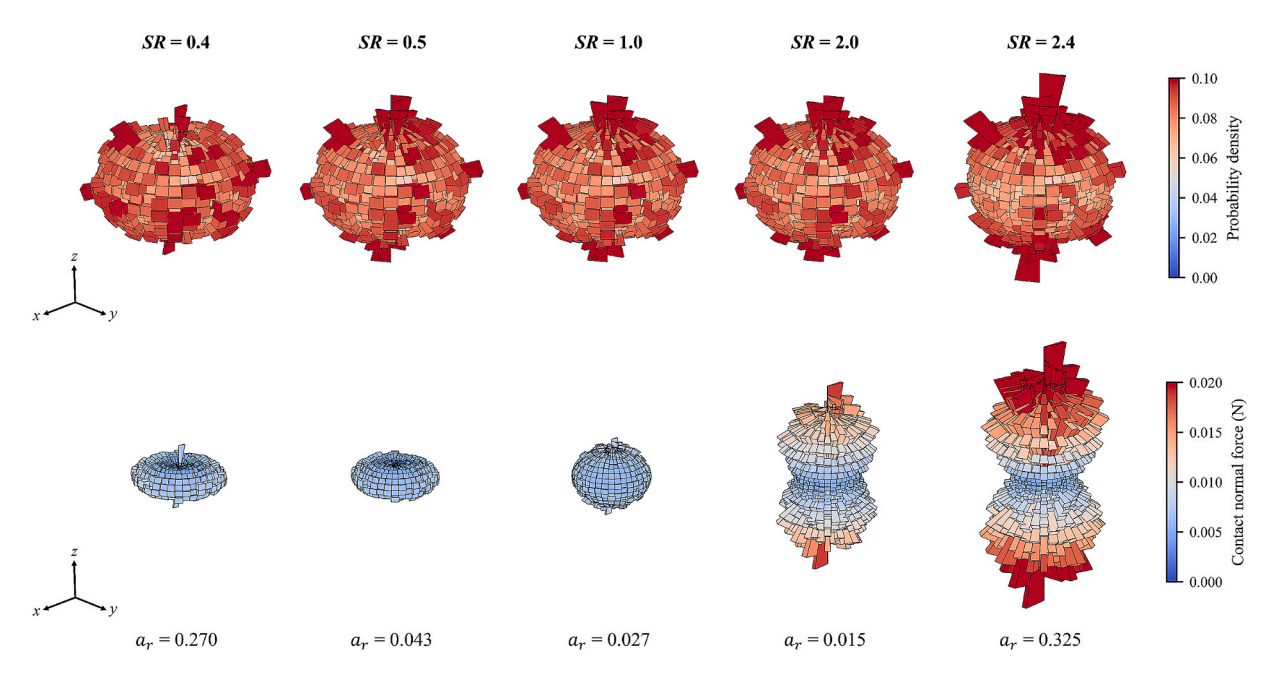


Fig. 6. Contact normal probability density and mean contact normal forces distribution in RTE-D1/CTC-D1 tests.

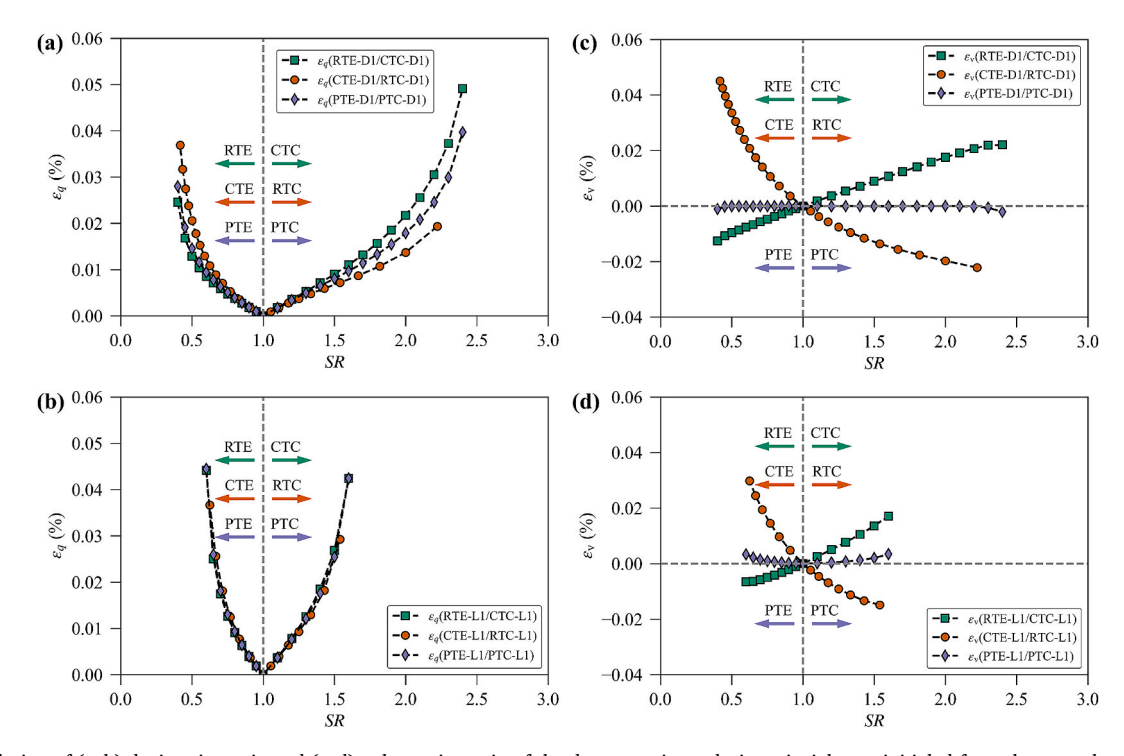


Fig. 7. Evolution of (a-b) deviatoric strain and (c-d) volumetric strain of the dense specimen during triaxial tests initialed from the stress level of 100 kPa.

these phenomena are not explicitly observed across all stress paths.

## 3.3. Comparison of empirical equations

Several empirical equations, notably Eqs. (2), (3), and (5) exist to illustrate the correlation between G and anisotropic stress states. In these equations, the stress level,  $[\sigma']$ , is taken as p',  $(\sigma'_i + \sigma'_j)/2$ , and  $\sqrt{\sigma'_i\sigma'_j}$ , respectively. We aim to evaluate the efficacy of these empirical equations across different stress paths. To begin, the factor,  $\Delta$ , was introduced, as a means to assess the extent of deviation of G/F(e) from its initial state at the onset of the triaxial tests:

$$\Delta_{ij} = \frac{G_{ij}/F(e)}{\left[G_{ij}/F(e)\right]_{\text{init}}} \tag{16}$$

where  $[G_{ij}/F(e)]_{init}$  is the initial  $G_{ij}/F(e)$ . As shown in Fig. 8,  $\Delta_{ij}$ measured in this study are compared with those predicted by different Equations. In spite of the stress path, the measured value starts to significantly deviate from the predicted values when SR exceeds its threshold range. This suggests that the SR effect observed in experiments mainly resulted from the substantial alteration in the fabric of the specimen, aligned with the perspective presented by Kuwano and Jardine (2002). Here, we use the term "SR effect" to describe the phenomenon where the measured  $\Delta_{ij}$  deviates from the predicted  $\Delta_{ij}$  as a result of increasing or decreasing SR value, respectively. In the RTE/CTC stress path, Chen and Yang (2024) observed that the SR effect on  $\Delta_{ar}$  (the subscript "a" and "r" indicate axial and radical direction in triaxial tests, respectively) is more remarkable in the extension case than in the compression case, regardless of the definition of  $[\sigma']$ . This finding is consistent within a specific SR range in this study, demonstrated in Fig. 9. Here, the experimental data used for  $\Delta_{\text{ar}}$  is derived from Ottawa sand with a void ratio of approximately 0.7 and an initial stress state of 200 kPa after Chen and Yang (2024).

Generally, within the threshold range of SR, the three definitions of  $[\sigma']$  result in the difference between the measured value and predicted value being approximately less than 10 %. Nevertheless, the predictive performance of using  $[\sigma'] = p'$  is notably poorer, particularly for the  $\Delta_{XY}$ 

in the RTE/CTC stress path. Using  $[\sigma']=\sqrt{\sigma'_i\sigma'_j}$  seems to be the optimal choice, as it results in the closest alignment between measured and predicted values across all stress paths when SR is within its threshold range. This might explain why the study of DEM commonly adopts  $[\sigma']=\sqrt{\sigma'_i\sigma'_j}$ . However, it is important to note that even when using  $[\sigma']=\sqrt{\sigma'_i\sigma'_j}$ , discrepancies still exist between the measured  $\Delta_{ij}$  and the predicted  $\Delta_{ij}$ . The extent of these discrepancies varies: in some stress paths and planes, they are substantial, while in others, they are minimal. These discrepancies can be clearly seen in Fig. 10, where the measured  $G_{ij}/F(e)$  is plotted against  $\sqrt{\sigma'_i\sigma'_j}$  for different stress paths within the threshold SR range. This implies that the redistribution of contact forces may also contribute to the SR effect, although its impact is relatively small compared to the fabric adjustment.

To quantify the extent to which the redistribution of contact forces contributes to the SR effect, we introduce a factor,  $R_c$ , as defined below:

$$R_{cij} = \frac{G_{ij}/F(e)/\left(\sqrt{\sigma'_{i}\sigma'_{j}}/p_{a}\right)^{1/3}}{\left[G_{ij}/F(e)/\left(\sqrt{\sigma'_{i}\sigma'_{j}}/p_{a}\right)^{1/3}\right]_{init}}$$
(17)

where the subscript "init" denotes the initial state from which a stress path initiated originates. Fig. 11 presents the SR effect on different planes during PTE-D1/PTC-D1 tests. During these tests, when SR lies within its threshold ranges, the specimen fabric remains nearly constant. Hence, the SR effect can be attributed to the redistribution of contact forces. The relationship between  $R_{\rm c}$  and SR is fitted by a power function for simplicity and avoid overfitting. In addition, because  $SR = \sigma'_{\rm v}/\sigma'_{\rm h}$ , and the denominator of Eq. (17) actually equal to the constant A, we can derive the equation below for CT, RT, and PT tests:

$$G_{ij} = AF(e) \left( \sqrt{\sigma'_i \sigma'_j} / p_a \right)^{1/3} \left( \sigma'_v / \sigma'_h \right)^{\beta}$$
(18)

where  $\beta$  is the *SR* exponent. In fact, Eq. (18) is an alternate form of Eqs. (4) and (6). Thus, when *SR* lies within its threshold range, *G* experiences

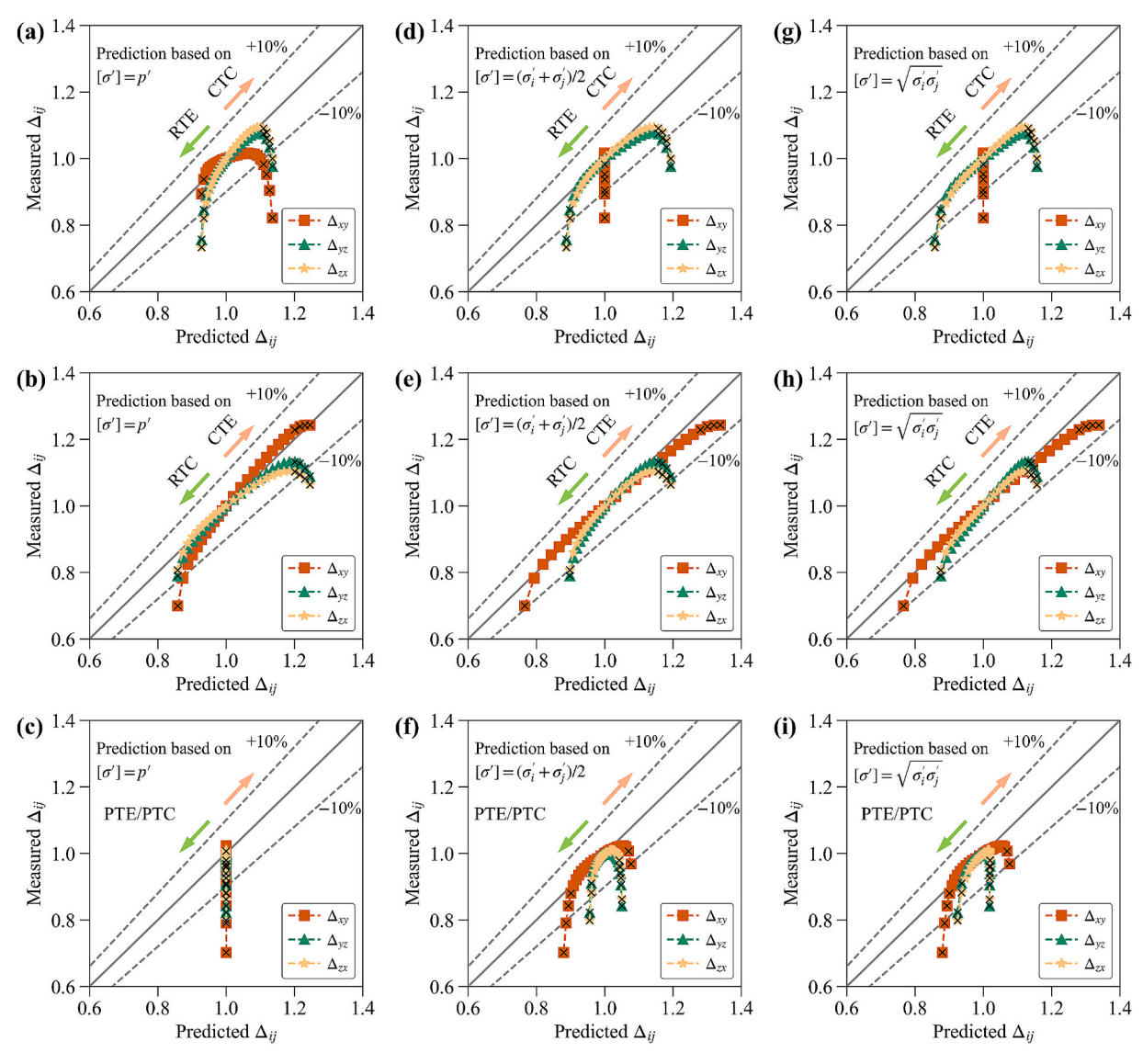


**Fig. 8.** Comparison of measured and predicted  $\Delta_{ij}$  during RTE-D1/CTC-D1, RTC-D1/CTE-D1, and PTE-D1/PTC-D1 tests for different  $[\sigma']$  definitions: (a–c)  $[\sigma'] = p'$ ; (d–f)  $[\sigma'] = (\sigma'_i + \sigma'_i)/2$ ; and (g–i)  $[\sigma'] = \sqrt{\sigma'_i \sigma'_i}$ . (Note: 'x' is affixed to the marker when *SR* exceeds its threshold values).

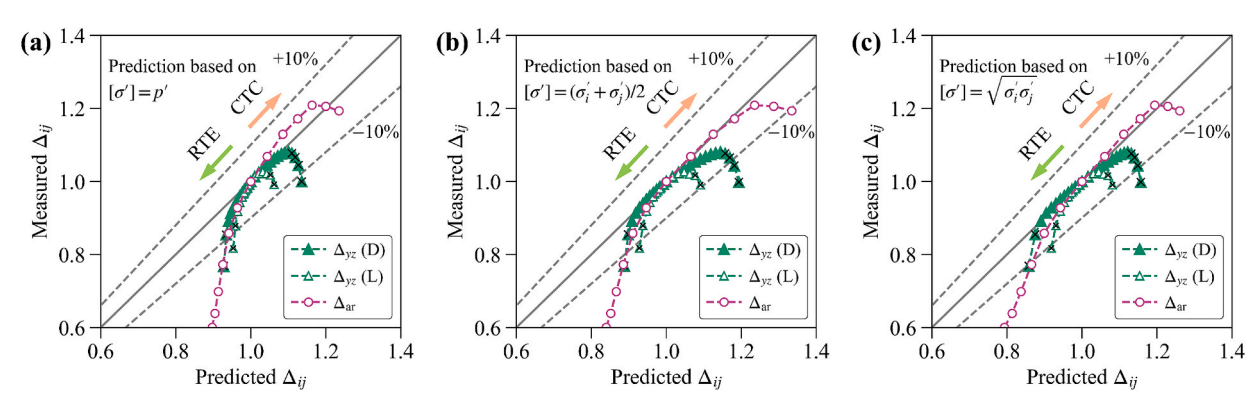
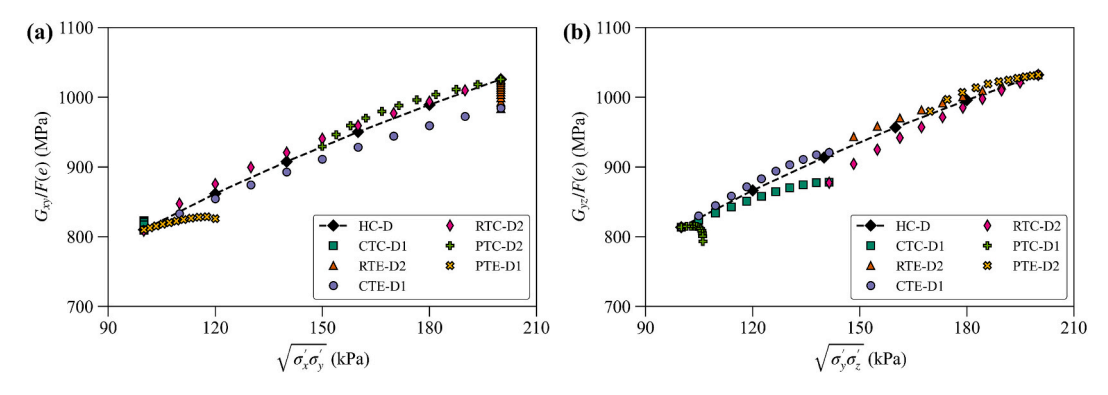


Fig. 9. Comparison of measured and predicted  $\Delta_{ij}$  ("D" indicates the dense specimen and "L" refers to the loose specimen; the experimental data of  $\Delta_{ar}$  is from Chen and Yang (2024)) during RTE/CTC tests initiated from an isotropic stress state of 200 kPa for different [σ'] definitions: (a) [σ'] = p'; (b) [σ'] = (σ'\_i + σ'\_j)/2; and (c) [σ'] =  $\sqrt{\sigma'_i\sigma'_j}$  (Note: 'x' is affixed to the marker when SR exceeds its threshold values).



**Fig. 10.** (a)  $G_{xy}/F(e)$  vs.  $\sqrt{\sigma_x'\sigma_y'}$  and (b)  $G_{yz}/F(e)$  vs.  $\sqrt{\sigma_y'\sigma_z'}$  in different stress paths within the threshold *SR* range.

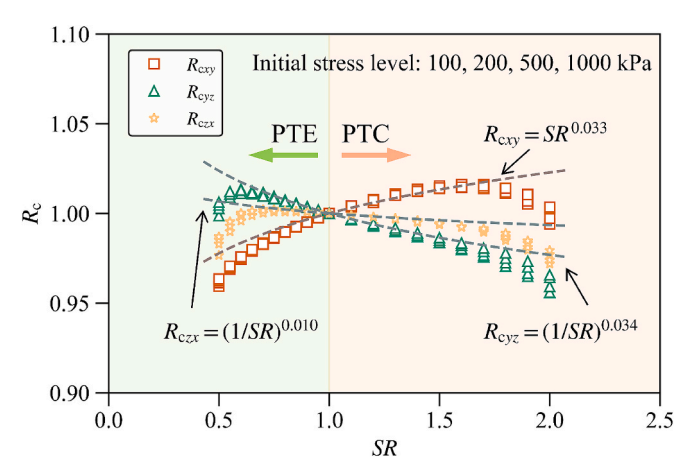


Fig. 11. Contribution of redistribution of contact forces to the SR effect.

a finite effect from the principal effective stress out-of-plane. In other words, Eqs. (4) and (6) are more accurate representations. However, it is important to acknowledge that excluding *SR* effect would only result in a minor discrepancy, which is generally within the experimental error range.

Furthermore, we define the normalized small-strain shear modulus, denoted as  $G_n$ , based on Eq. (18). The formulation is as follows:

$$G_{\text{n}ij} = G_{ij}/F(e)/\left(\sqrt{\sigma_i'\sigma_j'}/p_a\right)^{1/3}/(SR)^{\beta}$$
(19)

Theoretically,  $G_n$  should be approximate the constant A when SR is within its threshold range, considering that significant fabric adjustment is absent. The evolution of  $G_n$  in different stress paths is shown in Fig. 12. As expected, when SR is within its threshold range,  $G_n$  is nearly constant and equal on different planes, especially for the dense specimen. The variation in  $G_n$  for the loose specimen can be attributed to the slight reduction in  $Z_m$ .

## 3.4. Stiffness-stress-fabric relationship

When SR exceeds its threshold range during triaxial tests, G will

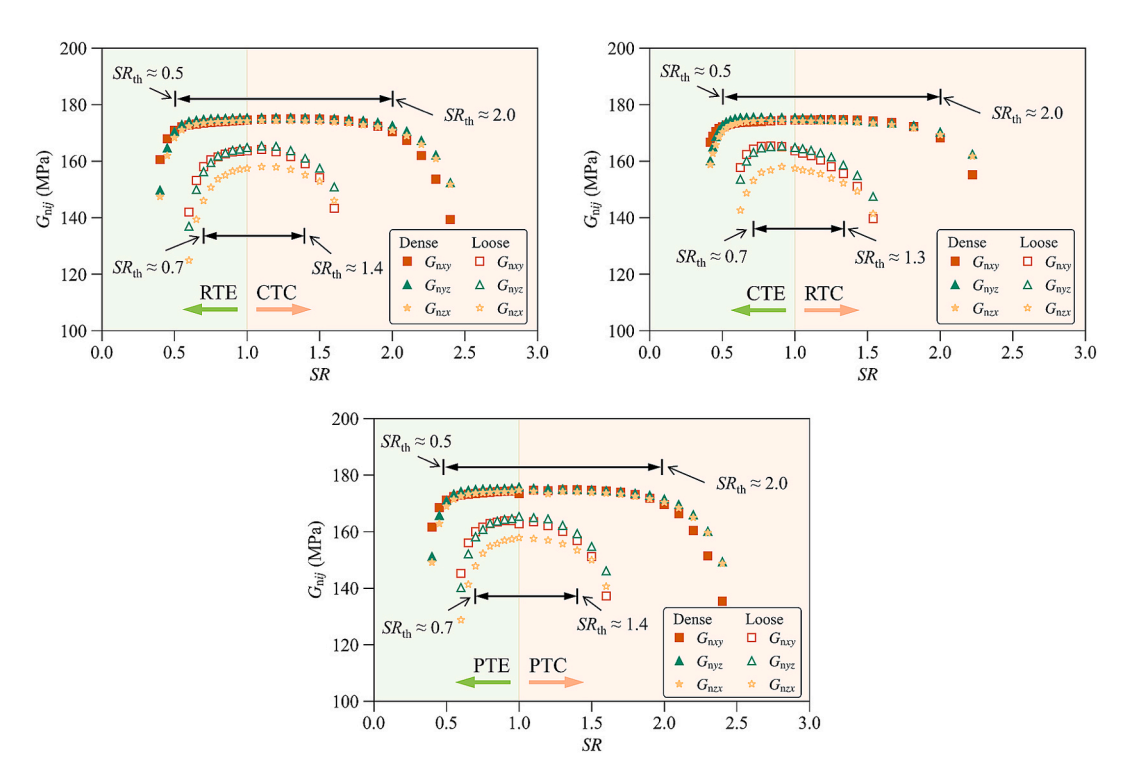


**Fig. 12.** Evolution of  $G_n$  ( $G_{ij}$  in MPa,  $\sqrt{\sigma_i'\sigma_j'}$  in kPa) during different triaxial tests: (a) RTE/CTC; (b) CTE/RTC; and PTE/PTC tests.

experience a significant SR effect, which primarily resulted from the adjustment of specimen fabric. To predict G across an extensive range of SR during triaxial tests, correction factors have been integrated into empirical equations, as indicated in previous studies (Yu and Richart, 1984; Payan et al., 2016; Chen and Yang, 2024). Nevertheless, these modified formulas are all phenomenological, and their application inevitably has limitations. Indeed, fabric information is indispensable to accurately predict G when SR exceeds its threshold range. Yet, unlike the linear correlation between  $G/\sigma_0^{-1/3}$  and  $(Z_m/e)^{2/3}$  at isotropic stress states, the relationship between small-strain shear modulus, anisotropic stress states and fabric has not been well established.

The shear stress in granular materials is primarily carried by "strong" contacts, which are those with contact forces greater than the average contact force (Radjai et al., 1998; Peters et al., 2005; Shi and Guo, 2018). Therefore, the "strong" contact networks form anisotropic structures that play an important role in the stiffness of granular materials. As shown in Fig. 13, the "strong" force chains are randomly oriented in isotropic stress states, displaying a relatively even probability density of  $F/\overline{F}$  in the HC stress path, where  $\overline{F}$  denotes the average contact force. However, the "strong" force chains are mainly oriented along the major principal stress direction in anisotropic stress states, and the triaxial loading reinforces the force inhomogeneity by increasing the relative probability densities of both "strong" and "weak" contact forces. This observation aligns consistently with previous findings (Antony, 2000; Richefeu et al., 2009). Furthermore, in the simplified Hertz-Mindlin contact model, the magnitude of the contact force also influences the contact stiffness, which in turn affects the macroscopic stiffness of the specimen. As a result, contacts with different contact forces contribute differently to the *G* of the specimen.

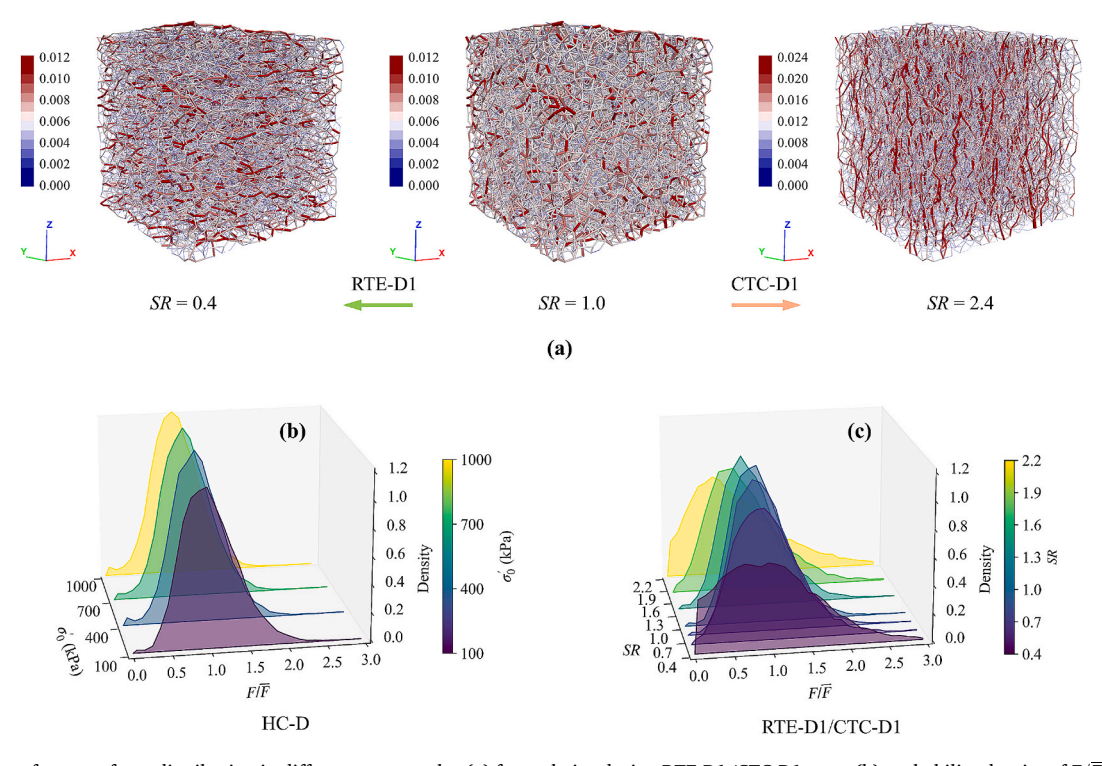
In line with Gu and Yang (2013), we utilized the weighted mechanical coordination number,  $Z_{\rm m}$ , to describe the "effective" connectivity of fabric that contributes to the G of the specimen. In calculating  $Z_{\rm m}$ , each contact is weighed by a factor given by  $(F/\overline{F})^{1/3}$ . If we simplify  $G_{ij}/\left(\sigma_i'\sigma_j'\right)^{1/6}/R_{cij}$  as shown in Fig. 14, we observe that  $G_{\rm nij}'$ 

 $\left(\Phi_{i}\Phi_{j}\right)^{1/2}$  has a strong linear relation to  $\left(Z_{\rm m}/e\right)^{2/3}$ . Here,  $\left(\Phi_{i}\Phi_{j}\right)^{1/2}$  accounts for the influence of fabric anisotropy. This linear relationship holds consistently under both isotropic and anisotropic stress states, demonstrating the universal dependence of the normalized shear modulus on the 'effective' connectivity and fabric anisotropy. This discovery may contribute to the development of more accurate constitutive models (e.g., Dafalias and Manzari, 2004), which account for fabric change effects, thereby enhancing our understanding and prediction of the mechanical behavior of granular materials.

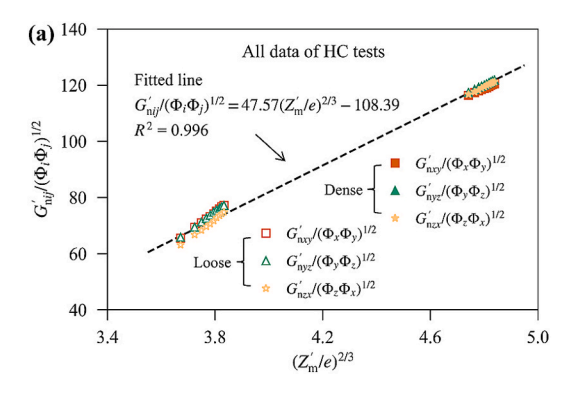
## 4. Conclusions

The evolution of the small-strain shear modulus (*G*) of granular materials during HC, CT, RT, and PT tests were studied utilizing 3D DEM. Empirical equations were analyzed in various stress paths by contrasting the predicted values with the actual measurements. Furthermore, an investigation was conducted into the relationship between small-strain shear modulus, stress states, and fabric. The key findings are summarized as follows:

- (a) In the HC stress path, G can be precisely estimated using Hardin's equation (Eq. (1)). Moreover, the stress-normalized small-strain shear modulus  $(G/\sigma_0'^{1/3})$ , exhibits a linear relationship with the function of mechanical coordination number and void ratio,  $(Z_m/e)^{2/3}$ , and the fabric of the specimen and distribution of contact normal forces are relatively uniform.
- (b) In CT, RT, and PT stress paths, the fabric of the specimen remains nearly unchanged within a threshold SR range. The differences between the measured G and predicted G using empirical equations, including Eqs. (2), (3), and (5), are roughly less than 10 % within this threshold SR range. The performance of Eq. (5) is the best. However, it should be noted that the principal effective stress out-of-plane has a finite effect on the G in a given plane. A factor,  $R_C$ , was introduced to evaluate the SR effect arising from



**Fig. 13.** Evolution of contact force distribution in different stress paths: (a) force chains during RTE-D1/CTC-D1 tests; (b) probability density of  $F/\overline{F}$  during the HC-D test; (c) probability density of  $F/\overline{F}$  during the RTE-D1/CTC-D1 tests.



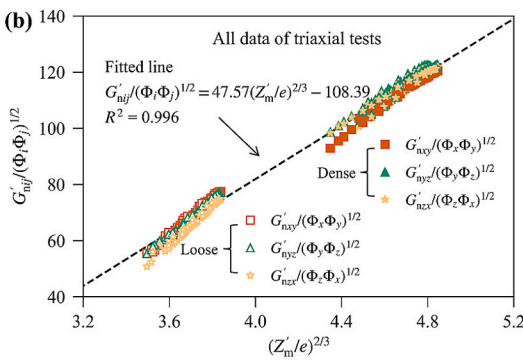


**Fig. 14.**  $G'_{\text{n}ij}/(\Phi_i\Phi_j)^{1/2}$  vs.  $(Z'_{\text{m}}/e)^{2/3}$  during (a) HC, (b) CT, RT, and PT tests  $(G_{ij}$  in MPa,  $\sigma'_0$  in kPa).

the redistribution of contact forces, which is fitted by the power function of *SR*.

(c) When SR surpasses its threshold range, G experiences a significant SR effect and the empirical function is no longer applicable, mainly resulting from the substantial adjustment of the specimen fabric. The fabric information is crucial for accurately predicting G when SR exceeds its threshold range. By incorporating the influence of redistribution of contact forces, "effective" connectivity of fabric, and fabric anisotropy into the empirical equation, the stiffness-stress-fabric relationship was established across a wide range of SR. This is demonstrated by the linear relationship between the function of weighted mechanical coordination,  $\left(Z_{\rm m}/e\right)^{2/3}$  and  $G_{ij}/\left(\sigma_i'\sigma_j'\right)^{1/6}/R_{\rm c}/\left(\Phi_i\Phi_j\right)^{1/2}$ .

It is to be noted that this study incorporates several simplifications, such as the assumption of spherical particles, which differ from real granular materials. To what extent such factors as particle morphology, physical properties and particle size distribution influence the findings presented here warrants further investigation.

## CRediT authorship contribution statement

**Mingjin Jiang:** Writing – original draft, Methodology, Investigation. **Jun Yang:** Writing – review & editing, Supervision, Methodology, Funding acquisition, Conceptualization.

## Declaration of competing interest

The authors declare that they have no known competing financial interests or personal relationships that could have appeared to influence the work reported in this paper.

## Acknowledgement

The financial support of the Research Grants Council of Hong Kong (17207923; N-HKU723/23; 17214724) is gratefully acknowledged.

## Data availability

Data will be made available on request.

## References

Andrus, R.D., Stokoe, K.H., 2000. Liquefaction resistance of soils from shear-wave velocity. J. Geotech. Geoenviron. Eng. 126 (11), 1015–1025. https://doi.org/ 10.1061/(ASCE)1090-0241(2000)126:11(1015).

Antony, S.J., 2000. Evolution of force distribution in three-dimensional granular media. PhysRevE 63 (1), 011302. https://doi.org/10.1103/PhysRevE.63.011302.

Barreto, D., O'Sullivan, C., Zdravkovic, L., 2009. Quantifying the evolution of soil fabric under different stress paths. AIP Conf. Proc. 1145 (1), 181–184. https://doi.org/ 10.1063/1.3179881. Bellotti, R., Jamiolkowski, M., LoPresti, D.C.F., ONeill, D.A., 1996. Anisotropy of small strain stiffness in Ticino sand. Géotechnique 46(1), 115–131. Doi: 10.1680/geot.1996.46.1.115.

Burland, J.B., Kalra, J.C., 1986. Queen Elizabeth II conference centre: geotechnical aspects. Proceedings-the Institution of Civil Engineers 80, 1479–1503.

Cha, M.S., Santamarina, J.C., Kim, H.S., Cho, G.C., 2014. Small-strain stiffness, shear-wave velocity, and soil compressibility. J. Geotech. Geoenviron. Eng. 140 (10). https://doi.org/10.1061/(ASCE)GT.1943-5606.0001157.

Chang, C.S., Chao, S.J., Chang, Y., 1995. Estimates of elastic-moduli for granular material with anisotropic random packing structure. Int. J. Solids Struct. 32 (14), 1989–2008. https://doi.org/10.1016/0020-7683(94)00225-L.

Chen, Y.T., Yang, J., 2024. Small-strain shear modulus of quartz sands under anisotropic stress conditions. J. Geotech. Geoenviron. Eng. 150 (5), 04024033. https://doi.org/ 10.1061/JGGEFK.GTENG-12160.

Clayton, C.R.I., Heymann, G., 2001. Stiffness of geomaterials at very small strains. Géotechnique 51 (3), 245–255. https://doi.org/10.1680/geot.51.3.245.39363.

Cundall, P.A., Jenkins, J.T., Ishibashi, I., 1989. Evolution of elastic moduli in a deforming granular assembly. In: Biarez, J., Gourves, R. (Eds.), Powders and Grains. Balkema, Rotterdam, pp. 319–322.

Cundall, P., Strack, O., 1979. A discrete numerical model for granual assemblies. Géotechnique 1 (979), 29. https://doi.org/10.1680/geot.1979.29.1.47.

da Cruz, F., Emam, S., Prochnow, M., Roux, J.N., Chevoir, F., 2005. Rheophysics of dense granular materials: Discrete simulation of plane shear flows. PhysRevE 72 (2), 021309. https://doi.org/10.1103/PhysRevE.72.021309.

Dafalias, Y.F., Manzari, M.T., 2004. Simple plasticity sand model accounting for fabric change effects. J. Eng. Mech. 130 (6), 622–634. https://doi.org/10.1061/(ASCE) 0733-9399(2004)130:6(622)

Dutta, T.T., Otsubo, M., Kuwano, R., 2021. Stress wave transmission and frequency-domain responses of gap-graded cohesionless soils. Soils Found. 61 (3), 857–873. https://doi.org/10.1016/j.sandf.2021.03.003.

Gong, J., Wang, X., Li, L., Nie, Z.H., 2019. DEM study of the effect of fines content on the small-strain stiffness of gap-graded soils. Comput. Geotech. 112, 35–40. https://doi. org/10.1016/j.compgeo.2019.04.008.

Gong, J., Pang, X.W., Tang, Y., Liu, M., Jiang, J., Ou, X.D., 2024. Effects of particle shape, physical properties and particle size distribution on the small-strain stiffness of granular materials: A DEM study. Comput. Geotech. 165, 105903. https://doi.org/10.1016/j.compgeo.2023.105903.

Gu, X.Q., Yang, J., Huang, M.S., 2013. DEM simulations of the small strain stiffness of granular soils: effect of stress ratio. Granular Matter 15 (3), 287–298. https://doi. org/10.1007/s10035-013-0407-y.

Gu, X.Q., Hu, J., Huang, M.S., 2017. Anisotropy of elasticity and fabric of granular soils. Granular Matter 19 (2). https://doi.org/10.1007/s10035-017-0717-6.

Gu, X.Q., Liang, X.M., Hu, J., 2023. Quantifying fabric anisotropy of granular materials using wave velocity anisotropy: A numerical investigation. Géotechnique. https:// doi.org/10.1680/jgeot.22.00314.

Gu, X.Q., Yang, J., 2013. A discrete element analysis of elastic properties of granular materials. Ganular Matter 15 (2), 139–147. https://doi.org/10.1007/s10035-013-0390-3

Guo, N., Zhao, J.D., 2013. The signature of shear-induced anisotropy in granular media. Comput. Geotech. 47, 1–15. https://doi.org/10.1016/j.compgeo.2012.07.002.

Hardin, B.O., Black, W.L., 1966. Sand stiffness under various triaxial stresses. J. Soil Mech. Found. Div. 92 (2), 27–42. https://doi.org/10.1061/JSFEAQ.0000865.

Hardin, B.O., Blandford, G.E., 1989. Elasticity of Particulate Materials. Int. J. Geotech. Eng. 115 (6), 788–805. https://doi.org/10.1061/(ASCE)0733-9410(1989)115:6 (788)

Hardin, B.O., Richart Jr, F., 1963. Elastic wave velocities in granular soils. J. Soil Mech. Found. Div. 89 (1), 33–65. https://doi.org/10.1061/JSFEAQ.0000493.

Hasan, A., Alshibli, K., 2012. Three dimensional fabric evolution of sheared sand. Granular Matter 14 (4), 469-482. https://doi.org/10.1007/s10035-012-0353-0.

Itasca, Particle flow code (PFC3D) manual. 2015. Itasca Consulting Group Inc. Minneapolis.

Iwasaki, T., Tatsuoka, F., 1977. Effects of grain size and grading on dynamic shear moduli of sands. Soils Found. 17 (3), 19–35. https://doi.org/10.3208/ sandf1972.17.3\_19.

- Jiang, M., Yang, J., 2024. Small-strain Young's modulus of granular materials at anisotropic stress states: A 3D DEM study. Powder Technol. 120249. https://doi.org/ 10.1016/j.powtec.2024.120249.
- Knox, D.P., Stokoe, K.H., Kopperman, S.E., 1982. Effect of state of stress on velocity of low-amplitude shear waves propagating along principal stress directions in dry sand. University of Texas at Austin.
- Kokusho, T., 1980. Cyclic triaxial test of dynamic soil properties for wide strain range. Soils Found. 20 (2), 45–60. https://doi.org/10.3208/sandf1972.20.2\_45.
- Kuribayashi, E., Iwasaki, T., Tatsuoka, F., 1975. Effects of stress-strain conditions on dynamic properties of sands. In Proceedings of the Japan Society of Civil Engineers. Japan Society of Civil Engineers, pp. 105–114. Doi: 10.2208/jscej1969.1975.242\_ 105.
- Kuwano, R., Jardine, R.J., 2002. On the applicability of cross-anisotropic elasticity to granular materials at very small strains. Géotechnique 52 (10), 727–749. https://doi. org/10.1680/geot.52.10.727.38848.
- Liu, X.Y., Li, Z.C., Zou, D.G., Sun, L.S., Yahya, K.E., Liang, J.M., 2023. Improving the prediction accuracy of small-strain shear modulus of granular soils through PSD: An investigation enabled by DEM and machine learning technique. Comput. Geotech. 157. https://doi.org/10.1016/j.compgeo.2023.105355.
- Magnanimo, V., La Ragione, L., Jenkins, J.T., Wang, P., Makse, H.A., 2008. Characterizing the shear and bulk moduli of an idealized granular material. Europhys. Lett. 81 (3). https://doi.org/10.1209/0295-5075/81/34006.
- Majmudar, T.S., Behringer, R.P., 2005. Contact force measurements and stress-induced anisotropy in granular materials. Nature 435 (7045), 1079–1082. https://doi.org/ 10.1038/nature03805.
- Mitaritonna, G., Amorosi, A., Cotecchia, F., 2014. Experimental investigation of the evolution of elastic stiffness anisotropy in a clayey soil. Géotechnique 64 (6), 463–475. https://doi.org/10.1680/geot.13.P.191.
- Ng, T.T., Petrakis, E., 1996. Small-strain response of random arrays of spheres using discrete element method. J. Eng. Mech. 122 (3), 239–244. https://doi.org/10.1061/ (ASCE)0733-9399(1996)122:3(239).
- Nguyen, H.C., O'Sullivan, C., Otsubo, M., 2018. Discrete element method analysis of small-strain stiffness under anisotropic stress states. Geotech. Lett. 8 (3), 183–189. https://doi.org/10.1680/jgele.17.00122.
- Nie, J.Y., Shi, X.S., Cui, Y.F., Yang, Z.Y., 2022. Numerical evaluation of particle shape effect on small strain properties of granular soils. Eng. Geol. 303, 106652. https:// doi.org/10.1016/j.enggeo.2022.106652.
- Oda, M., 1972. The mechanism of fabric changes during compressional deformation of sand. Soils Found, 12 (2), 1–18. https://doi.org/10.3208/sandf1972.12.1.
- sand. Soils Found. 12 (2), 1–18. https://doi.org/10.3208/sandf19/2.12.1. Oda, M., 1982. Fabric tensor for discontinuous geological materials. Soils Found. 22 (4), 96–108. https://doi.org/10.3208/sandf1972.22.4 96.
- O'Donovan, J., O'Sullivan, C., Marketos, G., Wood, D.M., 2015. Anisotropic stress and shear wave velocity: DEM studies of a crystalline granular material. Geotech. Lett. 5 (3), 224–230. https://doi.org/10.1680/igele.15.00032.
- Otsubo, M., Liu, J.M., Kawaguchi, Y., Dutta, T.T., Kuwano, R., 2020. Anisotropy of elastic wave velocity influenced by particle shape and fabric anisotropy under K<sub>0</sub> condition. Comput. Geotech. 128, 103775. https://doi.org/10.1016/j.compgeo.2020.103775.
- Payan, M., Khoshghalb, A., Senetakis, K., Khalili, N., 2016. Small-strain stiffness of sand subjected to stress anisotropy. Soil Dyn. Earthquake Eng. 88, 143–151. https://doi. org/10.1016/j.soildyn.2016.06.004.
- Perez, J.C.L., Kwok, C.Y., O'Sullivan, C., Huang, X., Hanley, K.J., 2016. Assessing the quasi-static conditions for shearing in granular media within the critical state soil mechanics framework. Soils Found. 56 (1), 152–159. https://doi.org/10.1016/j. sandf.2016.01.013.
- Peters, J.F., Muthuswamy, M., Wibowo, J., Tordesillas, A., 2005. Characterization of force chains in granular material. PhysRevE 72 (4). https://doi.org/10.1103/ PhysRevE.72.041307.
- Peyneau, P.E., Roux, J.N., 2008. Frictionless bead packs have macroscopic friction, but no dilatancy. PhysRevE 78 (1). https://doi.org/10.1103/PhysRevE.78.011307.
- Radjai, F., Wolf, D.E., Jean, M., Moreau, J.J., 1998. Bimodal character of stress transmission in granular packings. PhysRevLett. 80 (1), 61–64. https://doi.org/ 10.1103/PhysRevLett.80.61.
- Rampello, S., Viggiani, G.M.B., Amorosi, A., 1997. Small-strain stiffness of reconstituted clay compressed along constant triaxial effective stress ratio paths. Géotechnique 47 (3), 475–489. https://doi.org/10.1680/geot.1997.47.3.475.

- Richefeu, V., Youssoufi, M.S., Azéma, E., Radjaï, F., 2009. Force transmission in dry and wet granular media. Powder Technol. 190 (1–2), 258–263. https://doi.org/10.1016/i.powtec.2008.04.069.
- Roesler, S.K., 1979. Anisotropic Shear Modulus Due to Stress Anisotropy. J. Geotech. Eng. Div. 105 (7), 871–880. https://doi.org/10.1061/AJGEB6.0000835.
- Santamarina, J.C., Cascante, G., 1996. Stress anisotropy and wave propagation: A micromechanical view. Can. Geotech. J. 33 (5), 770–782. https://doi.org/10.1139/ t96-102-323.
- Satake, M., 1978. Constitution of mechanism of granular materials through graph representation. Theor. Appl. Mech. 26, 257–266.
- Saxena, S.K., Reddy, K.R., 1989. Dynamic moduli and damping ratios for Monterey No. 0 sand by resonant column tests. Soils Found. 29 (2), 37–51. https://doi.org/ 10.3208/sandf1972.29.2.37.
- Schmertmann, J.H., 1978. Effect of shear stress on dynamic bulk modulus of sand, No. 16. The Station.
- Schmidt, S., Wiebicke, M., Herle, I., 2022. On the determination and evolution of fabric in representative elementary volumes for a sand specimen in triaxial compression. Granular Matter 24 (4). https://doi.org/10.1007/s10035-022-01262-2.
- Shi, J.S., Guo, P.J., 2018. Fabric evolution of granular materials along imposed stress paths. Acta Geotech. 13 (6), 1341–1354. https://doi.org/10.1007/s11440-018-0665-2.
- Tatsuoka, F., Iwasaki, T., Fukushima, S., Sudo, H., 1979. Stress conditions and stress histories affecting shear modulus and damping of sand under cyclic loading. Soils Found. 19 (2), 29–43. https://doi.org/10.3208/sandf1972.19.2\_29.
- Thornton, C., 2000. Numerical simulations of deviatoric shear deformation of granular media. Géotechnique 50 (1), 43–53. https://doi.org/10.1680/geot.2000.50.1.43.
- van der Elst, N.J., Brodsky, E.E., Le Bas, P.Y., Johnson, P.A., 2012. Auto-acoustic compaction in steady shear flows: Experimental evidence for suppression of shear dilatancy by internal acoustic vibration. J. Geophys. Res.: Solid Earth 117(B9). Doi: 10.1029/2011jb008897.
- Wang, Y.H., Mok, C.M.B., 2008. Mechanisms of small-strain shear-modulus anisotropy in soils. J. Geotech. Geoenviron. Eng. 134 (10), 1516–1530. https://doi.org/10.1061/ (Asce)1090-0241(2008)134:10(1516).
- Wiącek, J., Marek, M., 2016. Representative elementary volume analysis of polydisperse granular packings using discrete element method. Particuology 27, 88–94. https:// doi.org/10.1016/j.partic.2015.08.004.
- Wiebicke, M., Ando, E., Viggiani, G., Herle, I., 2020. Measuring the evolution of contact fabric in shear bands with X-ray tomography. Acta Geotech. 15 (1), 79–93. https:// doi.org/10.1007/s11440-019-00869-9.
- Yang, J., Dai, B., 2011. Is the quasi-steady state a real behaviour? A micromechanical perspective. Géotechnique 61 (2), 175–183. https://doi.org/10.1680/geot.8.P.129.
- Yang, J., Yan, X.R., 2009. Site response to multi-directional earthquake loading: A practical procedure. Soil Dyn. Earthquake Eng. 29 (4), 710–721. https://doi.org/10.1016/j.soildvn.2008.07.008.
- Yang, J., 2024. Small is beautiful: Some new insights into small strain stiffness of granular soils. In: Recent Developments of Soil Mechanics and Geotechnics in Theory and Practice, Wichtmann, T., Machaček, J., Tafili, M. (eds), Lecture Notes in Applied and Computational Mechanics, vol 103. Springer. Doi: 10.1007/978-3-031-71896-0\_
- Yimsiri, S., Soga, K., 2010. DEM analysis of soil fabric effects on behaviour of sand. Géotechnique 60 (6), 483–495. https://doi.org/10.1680/geot.2010.60.6.483.
- Yu, P., Richart, F.E., 1984. Stress Ratio Effects on Shear Modulus of Dry Sands. Int. J. Geotech. Eng. 110 (3), 331–345. https://doi.org/10.1061/(ASCE)0733-9410(1984) 110:3(331)
- Zhang, L., Tang, X., Yang, J., 2023. Rainfall-induced flowslides of granular soil slopes: Insights from grain-scale modeling. Eng. Geol. 323. https://doi.org/10.1016/j. enggeo.2023.107223.
- Zhang, L., Yang, J., 2023. Grain-scale modeling of shear responses of dilative granular packings under stress path pertinent to rainfall-induced slope failures. Comput. Geotech. 162, 105671. https://doi.org/10.1016/j.compgeo.2023.105671.
- Zhou, Y.G., Chen, Y.M., 2007. Laboratory investigation on assessing liquefaction resistance of sandy soils by shear wave velocity. J. Geotech. Geoenviron. Eng. 133 (8), 959–972. https://doi.org/10.1061/(Asce)1090-0241(2007)133:8(959).